13 Nanostructures

The principles of physics,
as far as I can see,
do not speak against the possibility
of maneuvering things atom by atom.
R.P. Feynman, 1959 [859]

13.1 Introduction

When the structural size of functional elements enters the size range of the de Broglie matter wavelength, the electronic and optical properties are dominated by quantum-mechanical effects. The most drastic impact can be seen from the density of states (Fig. 13.1).

The quantization in a potential is ruled by the Schrödinger equation with appropriate boundary conditions. These are simplest if an infinite potential is assumed. For finite potentials, the wavefunction leaks out into the barrier. Besides making the calculation more complicated (and more realistic), this allows electronic coupling of nanostructures. Via the Coulomb interaction, a coupling is even given if there is no wavefunction overlap. In the following, we will discuss some of the fabrication techniques and properties of quantum wires (QWR) and quantum dots (QD). In particular for the latter, several textbooks can also be consulted [860, 861].

13.2 Quantum Wires

13.2.1 V-Groove Quantum Wires

Quantum wires with high optical quality, i.e. high recombination efficiency and well-defined spectra, can be obtained by employing epitaxial growth on corrugated substrates. The technique is shown schematically in Fig. 13.2. A V-groove is etched, using, e.g., an anisotropic wet chemical etch, into a GaAs substrate. The groove direction is along [110]. Even when the etched pattern is not very sharp on the bottom, subsequent growth of AlGaAs sharpens

M. Grundmann, *The Physics of Semiconductors*, 2nd ed., Graduate Texts in Physics, DOI 10.1007/978-3-642-13884-3_13,

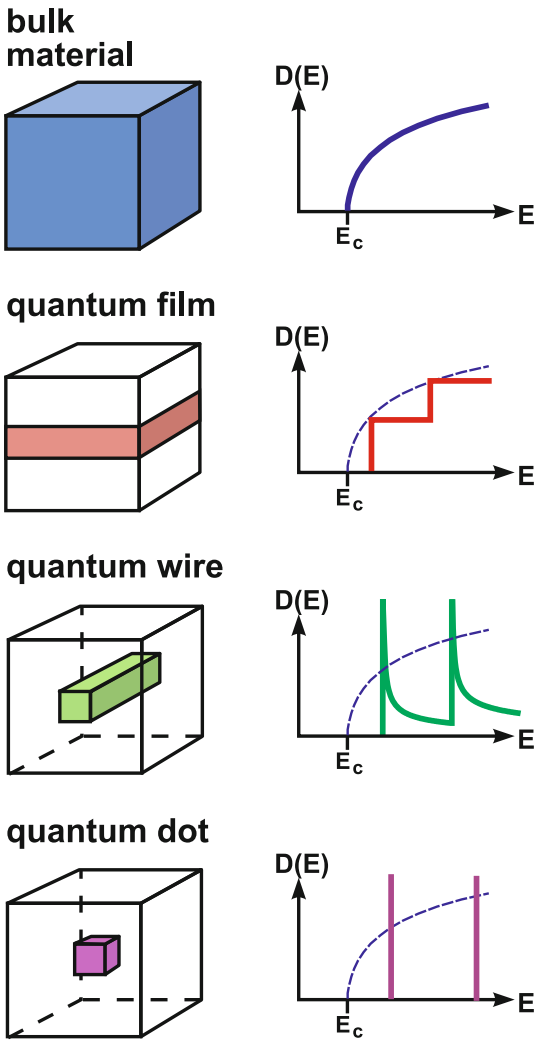

Fig. 13.1. Schematic geometry and density of states for 3D, 2D, 1D and 0D electronic systems

the apex to a self-limited radius ρ_l of the order of 10 nm. The side facets of the groove are {111}A. Subsequent deposition of GaAs leads to a larger upper radius $\rho_u > \rho_l$ of the heterostructure. The GaAs QWR formed in the bottom of the groove is thus crescent-shaped as shown in Fig. 13.3. A thin GaAs layer also forms on the side facets (sidewall quantum well) and on the top of the ridges. Subsequent growth of AlGaAs leads to a resharpening of the V-groove to the initial, self-limited value ρ_l. The complete resharpening after a sufficiently thick AlGaAs layer allows vertical stacking of crescent-

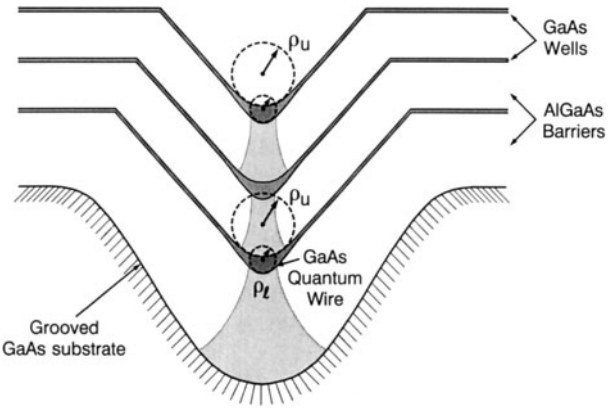

Fig. 13.2. Schematic cross section of a GaAs/AlGaAs heterostructure grown on a channeled substrate, illustrating the concept of self-ordered quantum-wire fabrication. Adapted from [862]

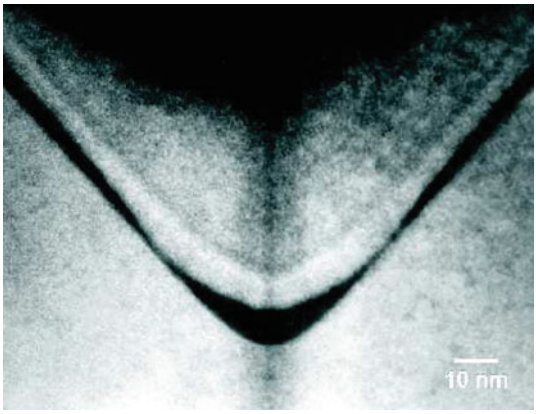

Fig. 13.3. Transmission electron microscopy cross-sectional image of a crescent-shaped single GaAs/AlGaAs quantum wire. From [863]

shaped QWRs of virtually identical size and shape, as shown in Fig. 13.4. In this sense, the self-limiting reduction of the radius of curvature and its recovery during barrier-layer growth leads to self-ordering of QWR arrays whose structural parameters are determined solely by growth parameters. The lateral pitch of such wires can be down to 240 nm.

To directly visualize the lateral modulation of the band gap, a lateral cathodoluminescence (CL) linescan perpendicular across the wire is displayed in Fig. 13.5. In Fig. 13.5a, the secondary electron (SE) image of the sample

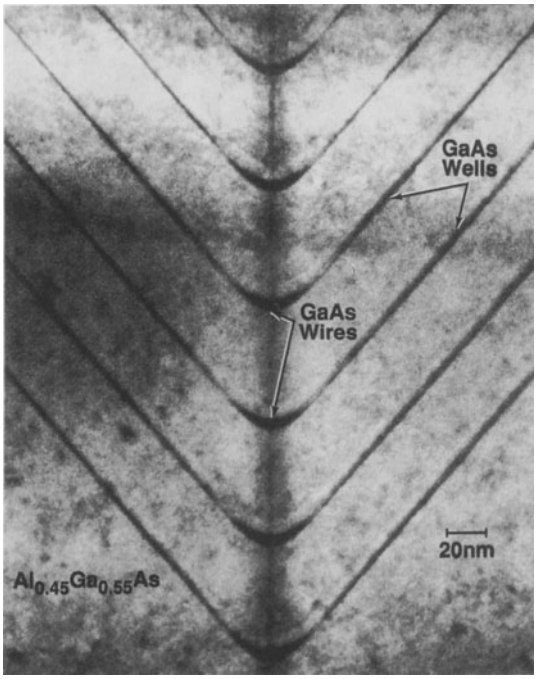

Fig. 13.4. TEM cross-sectional image of a vertical stack of identical GaAs/AlGaAs crescent-shaped QWRs. From [862]

from Fig. 13.3 is shown in plan view. The top ridge is visible in the upper and lower parts of the figure, while in the middle the sidewalls with the QWR in the center are apparent. In Fig. 13.5b, the CL spectrum along a linescan perpendicular to the wire (as indicated by the white line in Fig. 13.5a) is displayed. The x-axis is now the emission wavelength, while the y-axis is the lateral position along the linescan. The CL intensity is given on a logarithmic scale to display the full dynamic range. The top QW shows almost no variation in band gap energy ($\lambda = 725\,\text{nm}$); only directly at the edge close to the sidewall does a second peak at lower energy ($\lambda = 745\,\text{nm}$) appear, indicating a thicker region there. The sidewall QW exhibits a recombination wavelength of 700 nm at the edge to the top QW, which gradually increases to about 730 nm at the center of the V-groove. This directly visualizes a linear tapering of the sidewall QW from about 2.1 nm thickness at the edge to 3 nm in the center. The QWR luminescence itself appears at about 800 nm.

After fast capture from the barrier into the QWs and, to a much smaller extent corresponding to its smaller volume, into the QWR, excess carriers will diffuse into the QWR via the adjacent sidewall QW and the vertical QW. The tapering of the sidewall QW induces an additional drift current.

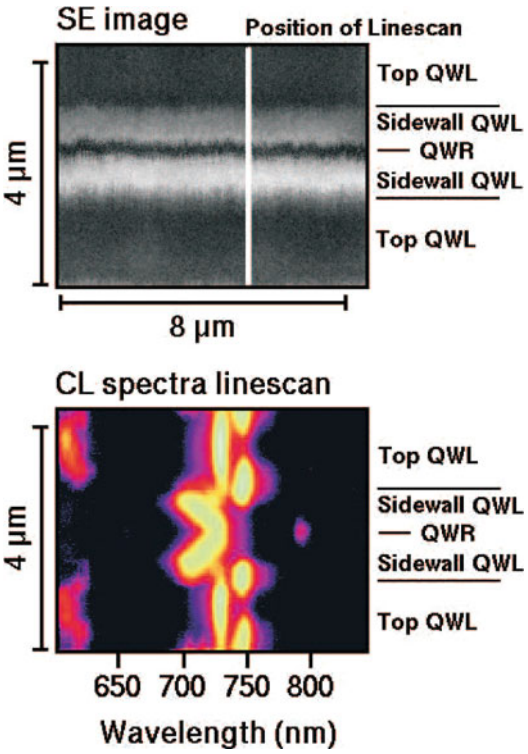

Fig. 13.5. (**a**) Plan-view SE image of single QWR (sample A), showing top and sidewall with QWR in the center. The *white line* indicates the position of the linescan on which the CL spectra linescan (**b**) has been taken at $T = 5\,\mathrm{K}$. The CL intensity is given on a logarithmic grey scale to display the full dynamic range as a function of wavelength and position along the *white line* in (**a**). From [863]

13.2.2 Cleaved-Edge Overgrowth Quantum Wires

Another method to create quantum wires of high structural perfection is cleaved-edge overgrowth (CEO) [864], shown schematically in Fig. 13.6. First, a layered structure is grown (single or multiple quantum wells or superlattice). Then, a {110} facet is fabricated by cleaving (in vacuum) and epitaxy is continued on the cleaved facet. At the junctures of the {110} layer and the original quantum wells QWRs form. Due to their cross-sectional form they are also called *T-shaped* QWRs. A second cleave and another growth step allow fabrication of CEO quantum dots [865, 866] (Fig. 13.6c).

13.2.3 Nanowhiskers

Whiskers are primarily known as thin metal spikes and have been investigated in detail [867]. Semiconductor whiskers can be considered as (fairly short) quantum wires. They have been reported for a number of materials, such as

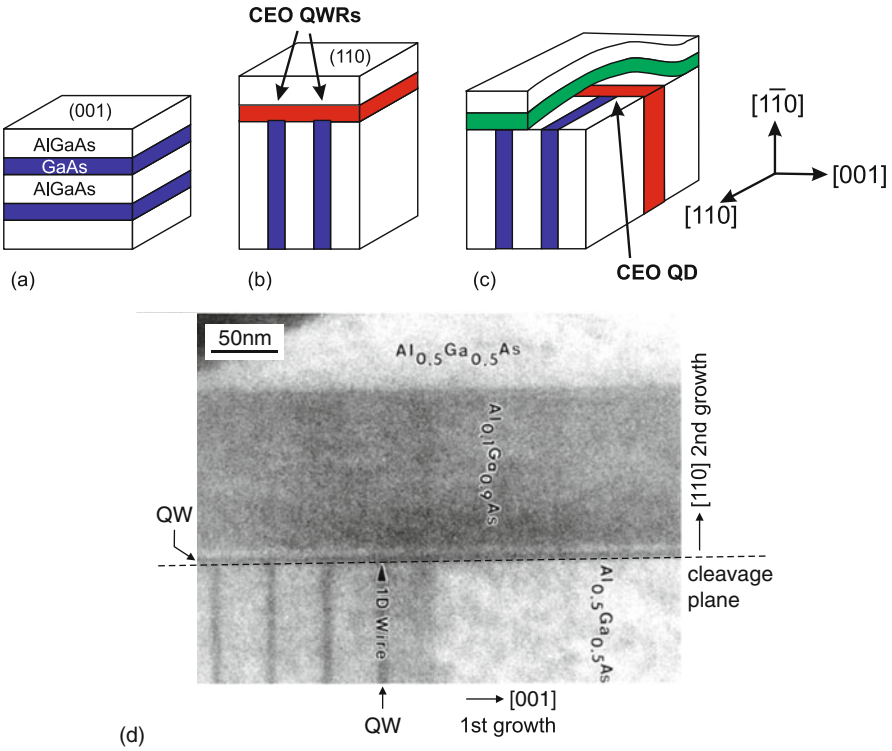

Fig. 13.6. Principle of CEO quantum wires and 2-fold CEO quantum dots. Part (**a**) depicts a layered structure (quantum wells or superlattice, *blue*), (**b**) describes the growth on the cleaved facet used for fabrication of quantum wires. In (**c**) a second cleave and growth on top of the plane allows the fabrication of quantum dots. From [865]. (**d**) Cross-sectional TEM image of CEO GaAs/AlGaAs quantum wires. Two quantum wells (QW) and the QWR at their junction are labeled. The first epitaxy was from left to right. The second epitaxy step was on top of the cleavage plane (*dashed line*) in the upward direction. Adapted from [866], reprinted with permission, ©1997 APS

Si, GaAs, InP and ZnO [868]. A field of ZnO whiskers is shown in Fig. 13.7. If heterostructures are incorporated along the whisker axis [869], quantum dots or tunneling barriers can be created (Fig. 13.8). The nanocrystal can also act as a nanolaser [870, 871]. In ZnO nanowhiskers the conversion of mechanical energy into electrical energy has been demonstrated [872] based on the piezoelectric effect (Sect. 14.4).

The critical thickness h_c in nanowire heterostructure is strongly modified from the 2D situation (Sect. 5.3.7). Based on the strain distribution of a misfitted slab in a cylindrical wire [875] the dependence of critical thickness on the nanowhisker radius r was developed [876, 877]. For given misfit ϵ there is a critical radius r_c for which h_c is infinite for $r < r_c$ (Fig. 13.9).

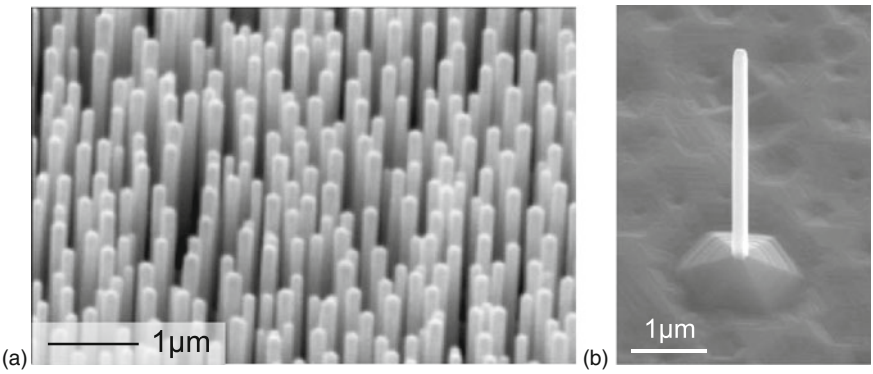

Fig. 13.7. (**a**) Array of ZnO nanowhiskers on sapphire, fabricated using thermal evaporation. Adapted from [873]. (**b**) Single, free-standing ZnO nanowire fabricated using PLD. Adapted from [874]

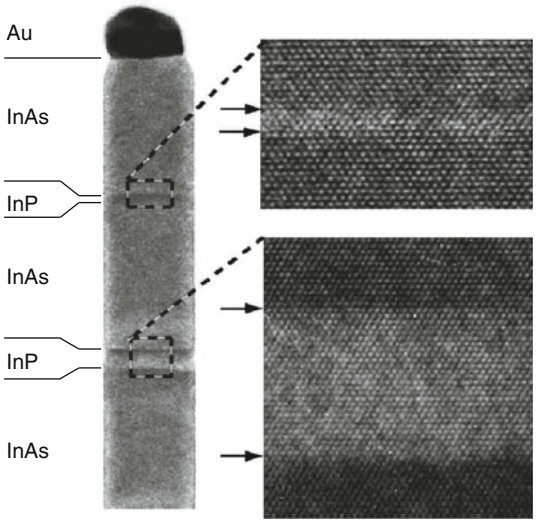

Fig. 13.8. TEM image of a part of an InAs whisker 40 nm in diameter that contains InP barriers. The zooms show sharp interfaces. On top of the whisker is a gold droplet from the so-called vapor–liquid–solid growth mechanism. The whisker axis is [001], the viewing direction is [110]. Adapted from [869], reprinted with permission, ©2002 AIP

13.2.4 Nanobelts

A number of belt-shaped nanostructures has been reported [868]. These are wire-like, i.e. very long in one dimension. The cross-section is rectangular with a high aspect ratio. In Fig. 13.10a ZnO nanobelts are shown. The wire direction is $[2\bar{1}.0]$. The large surface is (00.1), the thickness of the belt extends in [01.0]-direction. High resolution transmission microscopy (Fig. 13.10b) shows

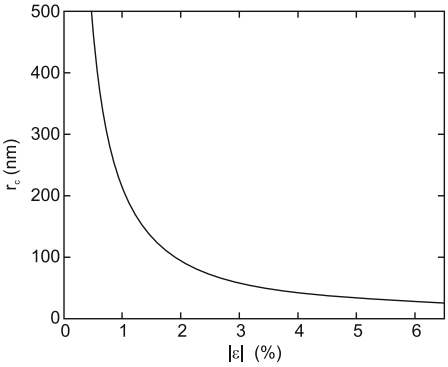

Fig. 13.9. Critical radius r_c above which an infinitely thick layer with misfit ϵ grows coherently on a cylindrical nanowire (relaxation by 60° dislocations, $b = 0.4\,\text{nm}$, $\nu = 1/3$). Adapted from [877]

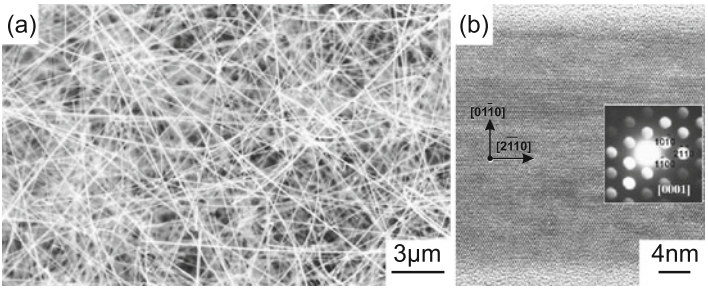

Fig. 13.10. (**a**) SEM image of an ensemble of ZnO nanobelts. (**b**) HRTEM image of a single ZnO nanobelt, viewing direction is [00.1]. The *inset* shows the diffraction pattern. Adapted from [878]

that these structures are defect-free. The pyroelectric charges on the ZnO (0001) surfaces (Sect. 14.2) lead to the formation of open (Fig. 13.11c) spirals. Closed spirals (Fig. 13.11a) occur if the short dimension is along [00.1] and alternating charges become compensated in a 'slinky'-like ring (Fig. 13.11b).

13.2.5 Quantization in Two-Dimensional Potential Wells

The motion of carriers along the quantum wire is free. In the cross-sectional plane the wavefunction is confined in two dimensions. The simplest case is for constant cross section along the wire. However, generally the cross section along the wire may change and therefore induce a potential variation along the wire. Such potential variation will impact the carrier motion along the longitudinal direction. Also, a twist of the wire along its axis is possible.

In Fig. 13.12, the electron wavefunctions in a V-groove GaAs/AlGaAs QWR are shown. Further properties of V-groove QWRs have been reviewed

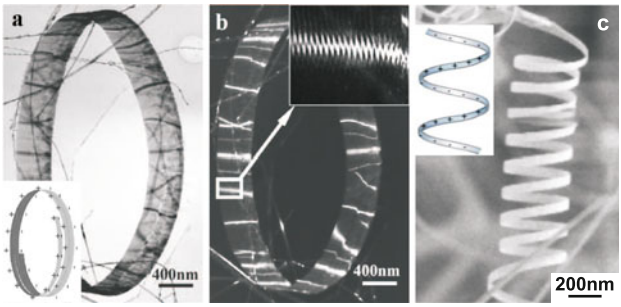

Fig. 13.11. (**a**) Bright field and (**b**) dark field TEM image of a ZnO nanoring formed by the 'slinky'-like growth of a nanobelt. (**c**) SEM image of an open ZnO nanospiral. The *insets* in (**a**, **c**) show schematically the surface charge distribution. Adapted from [879]

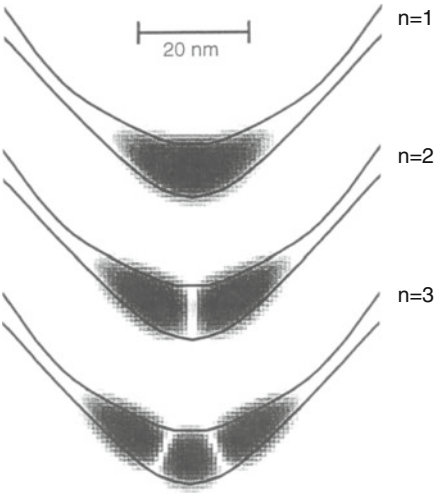

Fig. 13.12. Electron wavefunctions ($|\Psi|^2$ on logarithmic grey scale) for the first three confined levels for the QWR of Fig. 13.3. From [863]

in [880]. In Fig. 13.13, the excitonic electron and hole wavefunctions are shown for a (strained) T-shaped QWR.

In Fig. 13.14a the atomic structure of a very thin ZnO nanowhisker with a cross-section consisting of seven hexagonal unit cells is shown. The theoretical one-dimensional band structure [881] is shown in Fig. 13.14b together with the charge density of the lowest conduction band state (LUMO) and the highest valence band state (HOMO). The band gap is generally too small because of the LDA method used.[1] In [881] also the properties of nanowires

[1] The LDA in [881] yields $E_g = 0.63\,\text{eV}$ for the bulk ZnO band gap; its experimental value is 3.4 eV.

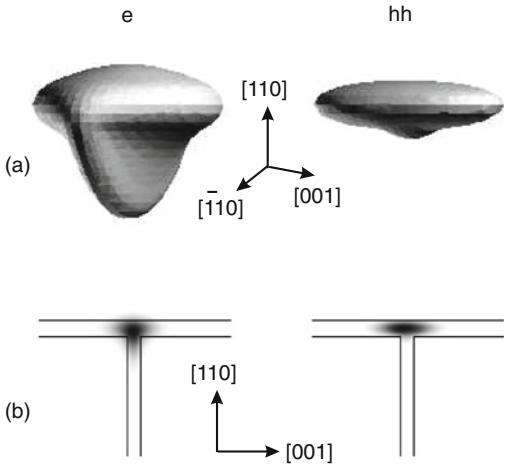

Fig. 13.13. (**a**) Three-dimensional view of the electron and (heavy) hole part of the excitonic wavefunction in a 4 nm × 5 nm T-shaped $In_{0.2}Ga_{0.8}As/GaAs$ QWR. The orbitals correspond to 70% probability inside. (**b**) Cross section through the electron and hole orbitals in their center along the wire direction. Reprinted with permission from [882], ©1998 APS

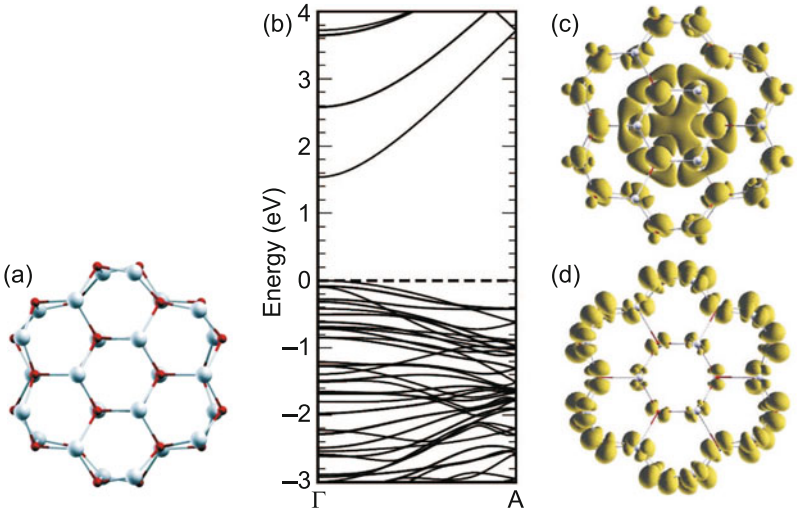

Fig. 13.14. (**a**) Atomic arrangement of a 1 nm wide ZnO nanowire. (**b**) Theoretical band structure and charge density of the (**c**) lowest conduction band and (**d**) highest valence band state. Adapted from [881]

with various diameters are compared. The HOMO at Γ lies only 80 meV above the top of valence band of bulk ZnO, and its position changes little with the wire diameter. It is mainly composed by surface oxygen 2p like dangling bonds (Fig. 13.14d). The LUMO ((Fig. 13.14c)) is delocalized in the whole nanowire, indicating that it is a bulk state. The delocalized distribution is also responsible for the large dispersion of the LUMO from Γ to A. The energy of the LUMO increases substantially with decreasing diameter due to the radial confinement.

13.3 Quantum Dots

13.3.1 Quantization in Three-Dimensional Potential Wells

The solutions for the d-dimensional ($d = 1$, 2, or 3) harmonic oscillator, i.e. the eigenenergies for the Hamiltonian

$$\hat{H} = \frac{\mathbf{p}^2}{2m} + \sum_{i=1}^{d} \frac{1}{2}\, m\, \omega_0^2\, x_i^2 \tag{13.1}$$

are given by

$$E_n = \left(n + \frac{d}{2}\right) \hbar\omega_0 \ , \tag{13.2}$$

with $n = 0, 1, 2, \ldots$. More detailed treatments can be found in quantum-mechanics textbooks.

Next, we discuss the problem of a particle in a centrosymmetric finite potential well with different masses m_1 in the dot and m_2 in the barrier. The Hamiltonian and the potential are given by

$$\hat{H} = \nabla \frac{\hbar^2}{2m} \nabla + V(r) \tag{13.3}$$

$$V(r) = \begin{cases} -V_0 \ , r \le R_0 \\ 0 \quad , r > R_0 \end{cases} \ . \tag{13.4}$$

The wavefunction can be separated into radial and angular components $\Psi(\mathbf{r}) = R_{nlm}(r)\ Y_{lm}(\theta, \phi)$, where Y_{lm} are the spherical harmonic functions. For the ground state ($n = 1$) the angular momentum l is zero and the solution for the wavefunction (being regular at $r = 0$) is given by

$$R(r) = \begin{cases} \frac{\sin(kr)}{kr} & , r \le R_0 \\ \frac{\sin(kR_0)}{kR_0}\ \exp\left(-\kappa(r - R_0)\right) & , r > R_0 \end{cases} \tag{13.5a}$$

$$k^2 = \frac{2m_1(V_0 + E)}{\hbar^2} \tag{13.5b}$$

$$\kappa^2 = -\frac{2m_2 E}{\hbar^2} \ . \tag{13.5c}$$

From the boundary conditions that both $R(r)$ and $\frac{1}{m}\frac{\partial R(r)}{\partial r}$ are continuous across the interface at $r = R_0$, the transcendental equation

$$kR_0 \cot(kR_0) = 1 - \frac{m_1}{m_2}(1 + \kappa R_0) \tag{13.6}$$

is obtained. From this formula the energy of the single particle ground state in a spherical quantum dot can be determined. For a given radius, the potential needs a certain strength $V_{0,\min}$ to confine at least one bound state; this condition can be written as

$$V_{0,\min} < \frac{\pi^2\hbar^2}{8m^*R_0^2} \tag{13.7}$$

for $m_1 = m_2 = m^*$. For a general angular momentum l, the wavefunctions are given by spherical Bessel functions j_l in the dot and spherical Hankel functions h_l in the barrier. Also, the transcendental equation for the energy of the first excited level can be given:

$$kR_0 \cot(kR_0) = 1 + \frac{k^2R_0^2}{\frac{m_1}{m_2}\frac{2+2\kappa R_0+\kappa^2R_0^2}{1+\kappa R_0} - 2} \,. \tag{13.8}$$

In the case of infinite barriers ($V_0 \to \infty$), the wavefunction vanishes outside the dot and is given by (normalized)

$$R_{nml}(r) = \sqrt{\frac{2}{R_0^3}}\frac{j_l(k_{nl}r)}{j_{l+1}(k_{nl}R_0)} \,, \tag{13.9}$$

where k_{nl} is the n-th zero of the Bessel function j_l, e.g. $k_{n0} = n\pi$. With two-digit precision the lowest levels are determined by

k_{nl}	$l=0$	$l=1$	$l=2$	$l=3$	$l=4$	$l=5$
$n=0$	3.14	4.49	5.76	6.99	8.18	9.36
$n=1$	6.28	7.73	9.10	10.42		
$n=2$	9.42					

The $(2l+1)$ degenerate energy levels E_{nl} are ($V_0 = \infty$, $m = m_1$):

$$E_{nl} = \frac{\hbar^2}{2m}\frac{k_{nl}^2}{R_0^2} \,. \tag{13.10}$$

The 1s, 1p, and 1d states have smaller eigenenergies than the 2s state.

A particularly simple solution is given for a cubic quantum dot of side length a_0 and infinite potential barriers. One finds the levels $E_{n_xn_yn_z}$:

$$E_{n_x n_y n_z} = \frac{\hbar^2}{2m}\,\pi^2\,\frac{n_x^2 + n_y^2 + n_z^2}{a_0^2}\,, \tag{13.11}$$

with n_x, n_y, $n_z = 1, 2, \ldots$. For a sphere, the separation between the ground and first excited state is $E_1 - E_0 \approx E_0$, for a cube and a two-dimensional harmonic oscillator it is exactly E_0. For a three-dimensional harmonic oscillator this quantity is $E_1 - E_0 = 2E_0/3$.

For realistic quantum dots a full three-dimensional simulation of strain, piezoelectric fields and the quantum-mechanical confinement must be performed [883, 884]. In Fig. 13.15, the lowest four electron and hole wavefunctions in a pyramidal InAs/GaAs quantum dot (for the strain distribution see Fig. 5.22 and for the piezoelectric fields see Fig. 14.16) are shown. The figure shows that the lowest hole states have dominantly heavy-hole character and contain admixtures of the other hole bands. The wavefunction in such quantum dots can be imaged using scanning tunneling microscopy [885].

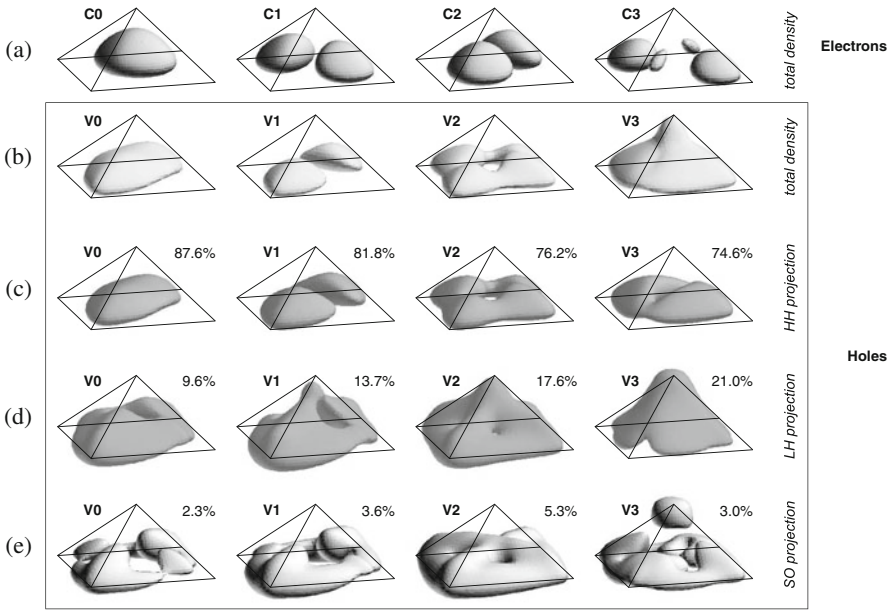

Fig. 13.15. Isosurface plots (25% of maximum value) of the total probability densities (**a**,**b**) and valence-band projections (**c**)–(**e**) of bound electron (**a**) and hole (**b**)–(**e**) states in a model pyramidal InAs/GaAs quantum dot with base length $b = 11.3\,\mathrm{nm}$. The percentages are the integrals of the projections to the bulk heavy, light and split-off hole bands, respectively, and the isosurfaces show the corresponding projection shapes. For each valence-band state the difference from 100% is the integral $\int_{-\infty}^{\infty} |\psi_{s\uparrow}|^2 + |\psi_{s\downarrow}|^2 \mathrm{d}^3\mathbf{r}$ of the s-type (conduction band) Bloch function projection (not shown). Reprinted with permission from [886]

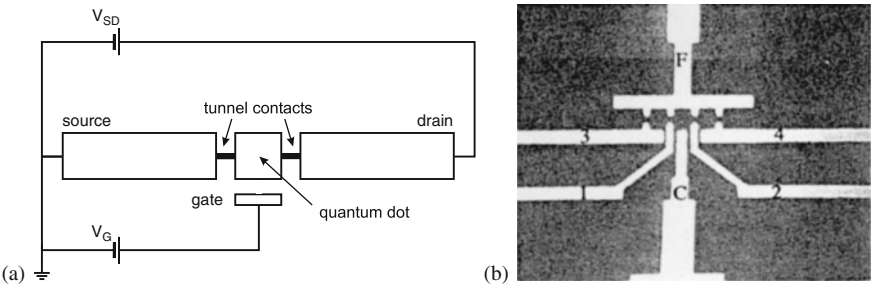

Fig. 13.16. (**a**) Schematic drawing of a quantum dot with tunnel contacts and gate electrode. (**b**) Realization with an in-plane gate structure. The distance between 'F' and 'C' (gate electrode) is 1 µm. Electron transport occurs from a 2DEG between 3/F to 4/F through the quantum points contacts 1/3 and 2/4. Part (**b**) reprinted with permission from [887]

13.3.2 Electrical and Transport Properties

The classical electrostatic energy of a quantum dot with capacitance C that is capacitively coupled to a gate (Fig. 13.16) at a bias voltage V_g is given by

$$E = \frac{Q^2}{2C} - Q\,\alpha\,V_\mathrm{g}\ , \tag{13.12}$$

where α is a dimensionless factor relating the gate voltage to the potential of the island and Q is the charge of the island.

Mathematically, minimum energy is reached for a charge $Q_\mathrm{min} = \alpha C V_\mathrm{g}$. However, the charge has to be an integer multiple of e, i.e. $Q = Ne$. If V_g has a value, such that $Q_\mathrm{min}/e = N_\mathrm{min}$ is an integer, the charge cannot fluctuate as long as the temperature is low enough, i.e.

$$kT \ll \frac{e^2}{2C}\ . \tag{13.13}$$

Tunneling into or out of the dot is suppressed by the Coulomb barrier $e^2/2C$, and the conductance is very low. Analogously, the differential capacitance is small. This effect is called *Coulomb blockade*. Peaks in the tunneling current (Fig. 13.17b), conductivity (Fig. 13.17a) and the capacitance occur, when the gate voltage is such that the energies for N and $N+1$ electrons are degenerate, i.e. $N_\mathrm{min} = N + \frac{1}{2}$. The expected level spacing is

$$e\,\alpha\,\Delta V_\mathrm{g} = \frac{e^2}{C} + \Delta\epsilon_N\ , \tag{13.14}$$

where $\Delta\epsilon_N$ denotes the change in lateral (kinetic) quantization energy for the added electron. e^2/C will be called the charging energy in the following. A variation of the source–drain voltage (for a given gate voltage) leads to a so-called Coulomb staircase since more and more channels of conductivity

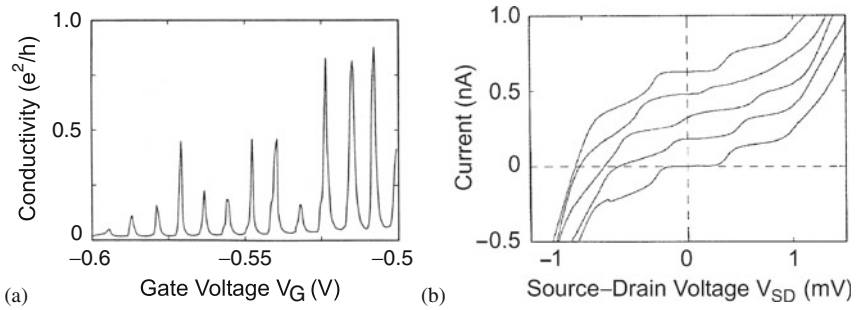

Fig. 13.17. (**a**) Conductivity (Coulomb oscillations) and (**b**) current–voltage diagram at different gate voltages (Coulomb staircase, shifted vertically for better readability) of a tunnel junction with a quantum dot as in Fig. 13.16. Adapted from [887]

contribute to the current through the device (Fig. 13.18). Single electron tunneling (SET) is investigated with respect to metrology for a novel ampere standard [845].

A lot of research so far has been done on lithographically defined systems where the lateral quantization energies are small and smaller than the Coulomb charging energy. In this case, periodic oscillations are observed, especially for large N. A deviation from periodic oscillations for small N and

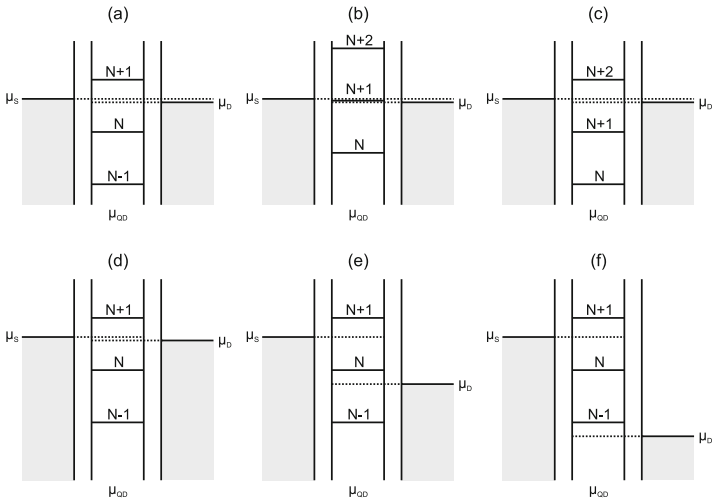

Fig. 13.18. Chemical potentials of source and drain and of a quantum dot in between them. (**a**), (**b**), and (**c**) show the sequence for a variation of the gate voltage and visualize the origin of the Coulomb oscillations (see Fig. 13.17a). (**d**), (**e**) and (**f**) visualize a variation of the source–drain voltage and the origin of the Coulomb staircase (cf. Fig. 13.17b)

a characteristic shell structure (at $N = 2, 6, 12$) consistent with a harmonic oscillator model ($\hbar\omega_0 \approx 3\,\text{meV}$) has been reported for ≈ 500-nm diameter mesas (Fig. 13.19b,c). In this structure, a small mesa has been etched and contacted (top contact, substrate back contact and side gate). The quantum dot consists of a 12-nm $In_{0.05}Ga_{0.95}As$ quantum well that is laterally constricted by the 500-nm mesa and vertically confined due to 9- and 7.5-nm thick $Al_{0.22}Ga_{0.68}As$ barriers (Fig. 13.19a). By tuning the gate voltage, the number of electrons can be varied within 0 and 40. Measurements are typically carried out at a sample temperature of 50 mK.

In the sample shown in Fig. 13.20, self-assembled QDs are positioned in the channel under a split-gate structure. In a suitable structure, tunneling through a single QD is resolved.

In small self-assembled quantum dots single-particle level separations can be larger than or similar to the Coulomb charging energy. Classically, the capacitance for a metal sphere of radius R_0 is given as

$$C_0 = 4\pi\,\epsilon_0\,\epsilon_r\,R_0\ , \tag{13.15}$$

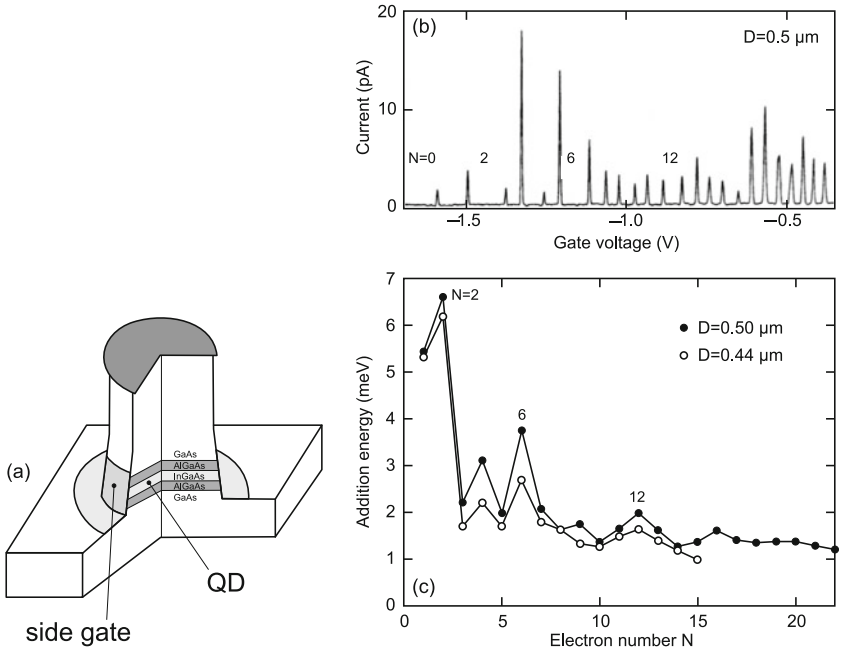

Fig. 13.19. (**a**) Schematic sample geometry for side-gated $In_{0.05}Ga_{0.95}As/Al_{0.22}Ga_{0.68}As$ disk-shaped quantum dot. (**b**) Coulomb oscillations in the current vs. gate voltage at $B = 0\,\text{T}$ observed for a $D = 0.5\,\mu\text{m}$ disk-shaped dot. (**c**) Addition energy vs. electron number for two different dots with $D = 0.50$ and $0.44\,\mu\text{m}$. Adapted from [888]

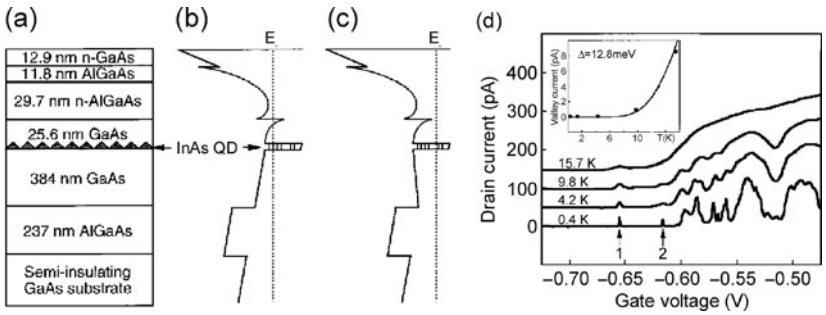

Fig. 13.20. (**a**) Schematic layer sequence of epitaxial structure comprising a n-AlGaAs/GaAs heterointerface with a two-dimensional electron gas and a layer of InAs/GaAs quantum dots. (**b**) and (**c**) are corresponding band diagrams with no gate bias and gate voltage below the critical value, respectively. (**d**) Experimental dependence of drain current on gate voltage in a split-gate structure at a drain source voltage of 10 µV. *Inset*: Dependence of valley current on temperature (*squares*) with theoretical fit. Reprinted with permission from [889], ©1997 AIP

e.g. $C_0 \approx 6\,\mathrm{aF}$ for $R_0 = 4\,\mathrm{nm}$ in GaAs, resulting in a charging energy of 26 meV. Quantum mechanically, the charging energy is given in first-order perturbation theory by

$$E_{21} = \langle 00|W_{\mathrm{ee}}|00\rangle = \iint \Psi_0^2(\mathbf{r}_\mathrm{e}^1)\, W_{\mathrm{ee}}(\mathbf{r}_\mathrm{e}^1, \mathbf{r}_\mathrm{e}^2)\, \Psi_0^2(\mathbf{r}_\mathrm{e}^2)\, \mathrm{d}^3\mathbf{r}_\mathrm{e}^1\, \mathrm{d}^3\mathbf{r}_\mathrm{e}^2\,, \qquad (13.16)$$

where W_{ee} denotes the Coulomb interaction of the two electrons and Ψ_0 the ground state (single particle) electron wavefunction. The matrix element gives an upper bound for the charging energy since the wavefunctions will rearrange to lower their overlap and the repulsive Coulomb interaction. For lens-shaped InAs/GaAs quantum dots with radius 25 nm a charging energy of about 30 meV has been predicted.

13.3.3 Self-assembled Preparation

The preparation methods for QDs split into top-down (lithography and etching) and bottom-up (self-assembly) methods. The latter achieve typically smaller sizes and require less effort (at least concerning the machinery).

Artificial Patterning

Using artificial patterning, based on lithography and etching (Fig. 13.21), quantum dots of arbitrary shape can be made (Fig. 13.22). Due to defects introduced by high-energy ions during reactive ion etching the quantum efficiency of such structures is very low when they are very small. Using wet-chemical etching techniques the damage can be significantly lowered but not completely avoided. Since the QDs have to compete with other structures that can be made structurally perfect, this is not acceptable.

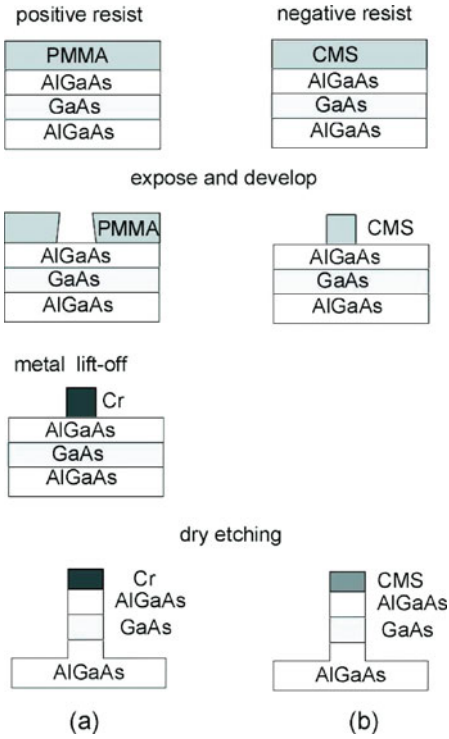

Fig. 13.21. Lithography and etching techniques for the fabrication of semiconductor structures

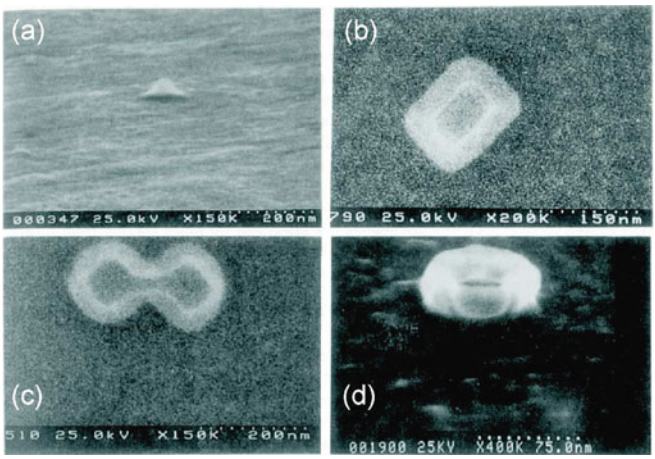

Fig. 13.22. Quantum dots of various shapes created by lithography and etching techniques. From [890]

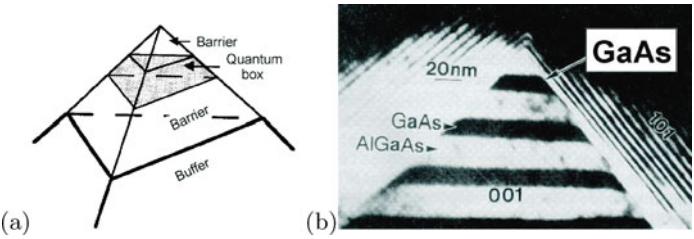

Fig. 13.23. (**a**) Schematic representation of growth on top of a predefined template, (**b**) cross-sectional TEM of quantum dot formation at the apex. Reprinted with permission from [891], ©1992 MRS

Template Growth

Template growth is another technique for the formation of nanostructures. Here, a mesoscopic structure is fabricated by conventional means. The nanostructure is created using size-reduction mechanisms, e.g. faceting, (Fig. 13.23). This method can potentially suffer from low template density, irregularities of the template, and problems of reproducibility.

Colloids

Another successful route to nanocrystals is the doping of glasses with subsequent annealing (color filters). When nanocrystals are prepared in a sol-gel process, the nanoparticles are present as a colloid in wet solution (Fig. 13.24). With the help of suitable stabilizing agents they are prevented from sticking to each other and can be handled in ensembles and also individually.

Mismatched Epitaxy

The self-assembly (or self-organization) relies on strained heterostructures that achieve energy minimization by island growth on a wetting layer (Stranski-Krastanow growth mode, see Sect. 11.2.3 and [860]). Additional ordering

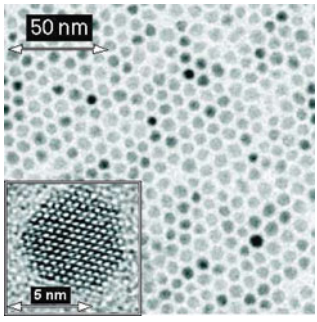

Fig. 13.24. CdSe colloidal nanoparticles. From [892]

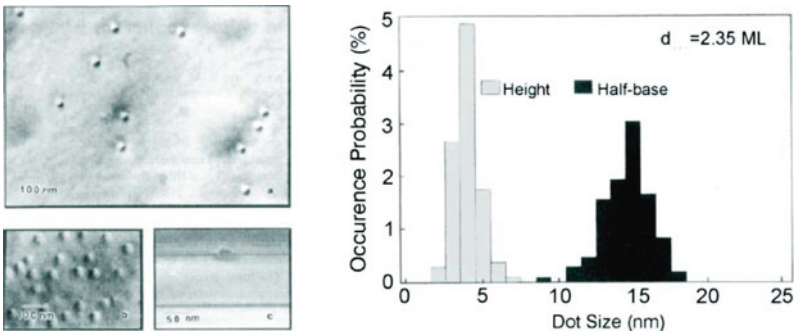

Fig. 13.25. Self-organized formation of InGaAs/GaAs quantum dots during epitaxy. *Left*: Plan-view and cross-sectional transmission electron micrographs. *Right*: Histogram of vertical and lateral size of the quantum dots. Reprinted with permission from [897], ©1993 AIP

mechanisms [893, 894] lead to ensembles that are homogeneous in size[2] [895] and shape [896] (Fig. 13.25).

When a thin layer of a semiconductor is grown on top of a flat substrate with different lattice constant, the layer suffers a tetragonal distortion (Sect. 5.3.3). Strain can only relax along the growth direction (Fig. 13.26). If the strain energy is too large (highly strained layer or large thickness), plastic relaxation via dislocation formation occurs. If there is island geometry, strain can relax in all three directions and about 50% more strain energy can relax,

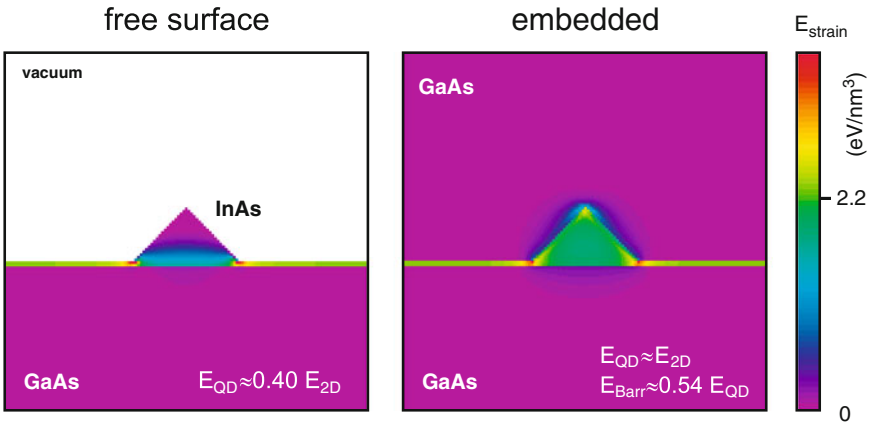

Fig. 13.26. Distribution of strain energy for (*left*) uncapped island and (*right*) island embedded in host matrix. Numerical values are for InAs/GaAs

[2]The ordering in size is remarkable. Typically Ostwald ripening (due to the Gibbs-Thomson effect; smaller droplets have larger vapor pressure and dissolve, larger droplets accordingly grow) occurs in an ensemble of droplets or nuclei. In the case of strained QDs, surface energy terms stabilize a certain QD size.

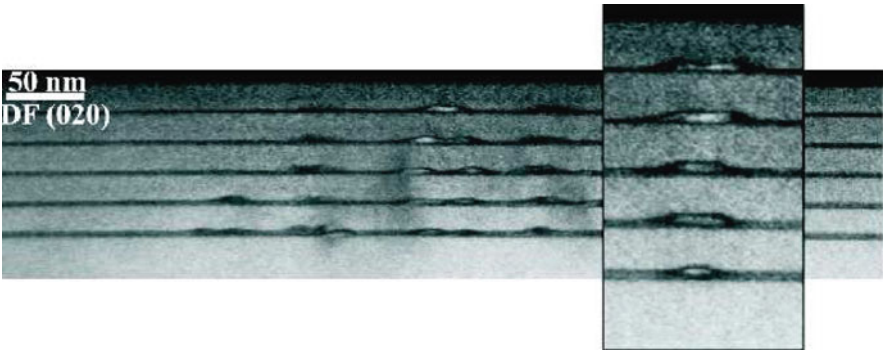

Fig. 13.27. Cross-sectional TEM image of a stack of five layers of quantum dots. Due to strain effects, vertical arrangement is achieved

thus making this type of relaxation energetically favorable. When the island is embedded in the host matrix, the strain energy is similar to the 2D case and the matrix becomes strained (metastable state).

When such QD layers are vertically stacked, the individual quantum dots grow on top of each other (Fig. 13.27) if the separation is not too large (Fig. 13.29). This effect is due to the effect of the underlying QD. In the case of InAs/GaAs (compressive strain), the buried QD stretches the surface above it (tensile surface strain). Thus, atoms impinging in the next QD layer find a smaller strain right on top of the buried QDs. In STM images of the cross section through (XSTM) such a stack (Fig. 13.28) individual indium atoms are visible and the shape can be analyzed in detail [898].

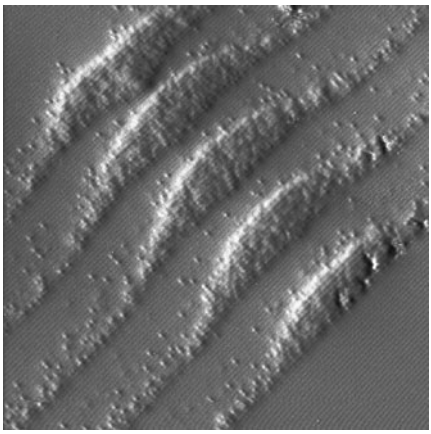

Fig. 13.28. Cross-sectional STM image of a stack of five InAs quantum dots in a GaAs matrix. Individual In atoms can be observed in-between the wetting layers and the quantum dots. Each quantum dot layer was formed by growing 2.4 ML of InAs. The intended distance between the quantum dot layers was 10 nm. Image size is $55 \times 55\,\mathrm{nm}^2$. Reprinted with permission from [898], ©2003 AIP

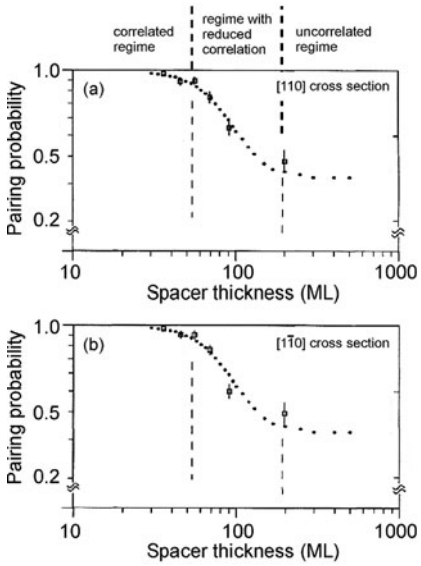

Fig. 13.29. Experimentally observed pairing probability in MBE-grown stacks of InAs/GaAs quantum dots as a function of the spacer-layer thickness. Data are taken from (**a**) (110) and (**b**) (1–10) cross-sectional TEM images. The *filled circles* are fit to data from theory of correlated island formation under strain fields. Reprinted with permission from [899], ©1995 APS

The vertical arrangement can lead to further ordering since a homogenization in lateral position takes place. If two QDs in the first layers are very close, their strain fields overlap and the second layer 'sees' only one QD.

The lateral (in-plane) ordering of the QDs with respect to each other occurs in square or hexagonal patterns and is mediated via strain interaction through the substrate. The interaction energy is fairly small, leading only to short-range in-plane order [893] as shown in Fig. 13.30. The in-plane ordering can be improved up to the point that regular one- or two-dimensional arrays form or individual quantum dots are placed on designated positions using directed self-assembly [860]. Among others, dislocation networks buried under the growth surface of the nanostructure, surface patterning and modification have been used to direct the QD positioning.

Ion-Beam Erosion

During the erosion of a surface with low-energy ion beam sputtering ordered patterns of dots appear [900–903]. Isotropic [904] and hexagonal [900, 902] (Fig. 13.31) near-range ordering has been observed. The pattern formation mechanism is based on the morphology-dependent sputter yield and further mechanisms of mass redistribution [905]. Also linear patterns have been reported [906].

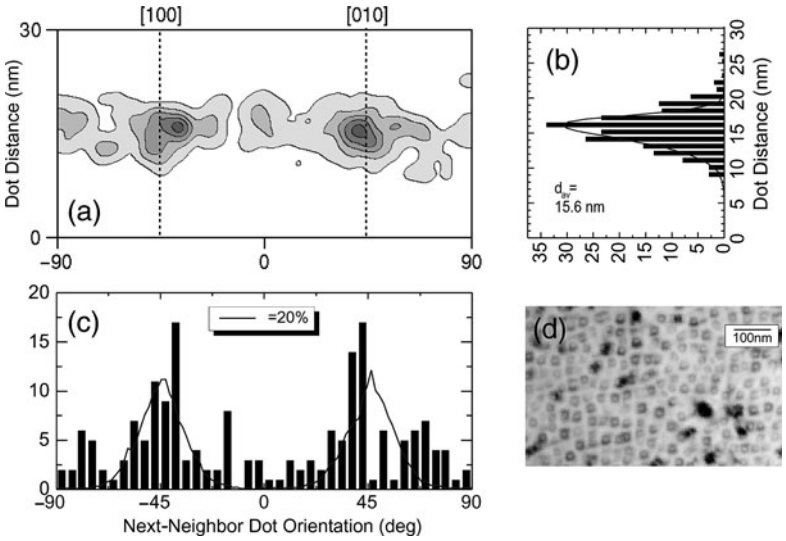

Fig. 13.30. Lateral ordering of QD array. (**d**) Plan-view TEM of QD array on which the statistical evaluation is based. (**a**) Two-dimensional histogram of QDs as a function of the nearest-neighbor distance and direction, (**b**,**c**) projections of part (**a**). *Solid lines* in (**b**) and (**c**) are theory for square array with $\sigma = 20\%$ deviation from ideal position. Adapted from [860] and [894]

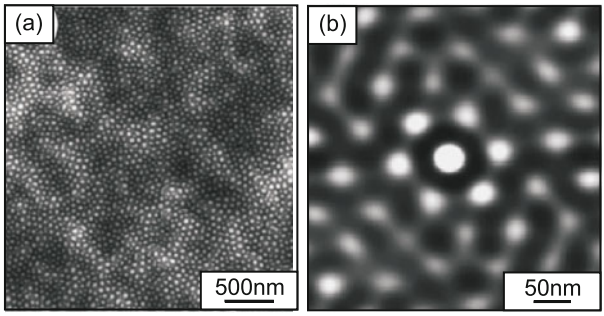

Fig. 13.31. (**a**) AFM image of a Si (001) substrate after 960 min of ion sputtering (1.2 keV Ar^+, normal incidence). (**b**) Two-dimensional autocorrelation function from a $400 \times 400\,nm^2$ area of image in part (**a**). Adapted from [902]

13.3.4 Optical Properties

The optical properties of QDs are related to their electronic density of states. In particular, optical transitions are allowed only at discrete energies due to the zero-dimensional density of states.

Photoluminescence from a single QD is shown in Fig. 13.32. The δ-like sharp transition is strictly true only in the limit of small carrier numbers ($\ll 1$ exciton per dot on average) since otherwise many-body effects come into play

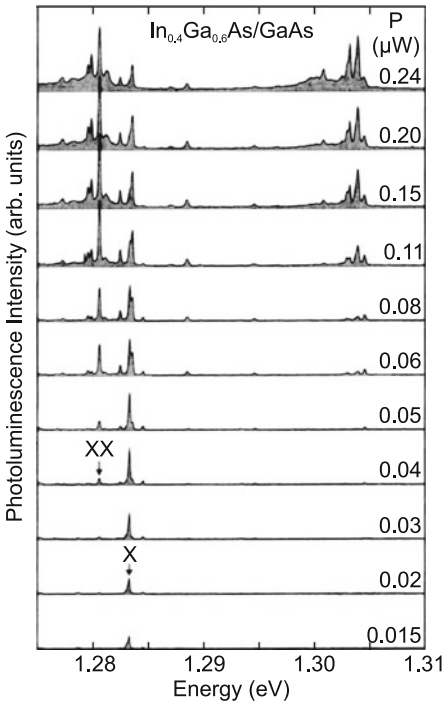

Fig. 13.32. Optical emission spectra ($T = 2.3\,\mathrm{K}$) of a single InGaAs/GaAs quantum dot at different laser excitation levels P as labeled. The single exciton (X) and biexciton (XX) lines are indicated. Adapted from [911]

that can encompass recombination from charged excitons or multiexcitons. At very low excitation density the recombination spectrum consists only of the one-exciton (X) line. With increasing excitation density small satellites on either side of the X-line develop that are attributed to charged excitons (trions) X^+ and X^-. On the low-energy side, the biexciton (XX) appears. Eventually, the excited states are populated and a multitude of states contribute with rich fine structure. In bulk material the biexciton (Sect. 9.5.11) is typically a bound state, i.e. its recombination energy E_{XX} is lower than that of the exciton E_X. A similar situation is present in Fig. 13.32. It was pointed out in [907] that in QDs the biexciton recombination energy can also be *larger* than the exciton recombination energy. In [908] the modification of the QD confinement potential of InAs/GaAs QDs by annealing was reported. The exciton binding energy (E_X-E_{XX}) is tuned from positive ('normal') to negative values upon annealing (Fig. 13.33).

The charging state of the exciton can be controlled in a field-effect structure. The recombination energy is modified due to Coulomb and exchange effects with the additional carriers. In charge-tunable quantum dots [909] and rings [910] exciton emission has been observed in dependence of the

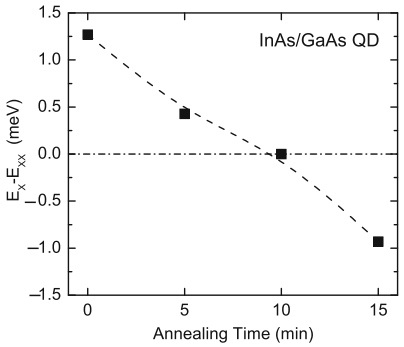

Fig. 13.33. Biexciton binding energy determined for a single InAs/GaAs quantum dot for various annealing times. Data from [908]

number of additional electrons. The electron population can be controlled in a Schottky-diode-like structure through the manipulation of the Fermi level with the bias voltage. At high negative bias all charge carriers tunnel out of the ring and no exciton emission is observed. A variation of the bias then leads to an average population with $N = 1, 2, 3, \ldots$ electrons. The recombination of additional laser-excited excitons depends (due to the Coulomb interaction) on the number of the electrons present (Fig. 13.34). The singly negatively charged exciton X^- is also called a trion.

The interaction of a spin with an exciton in a CdTe quantum dot has been observed in [912]. If the CdTe quantum dot is pure, a single line arises. If the dot contains a single Mn atom, the exchange interaction of the exciton

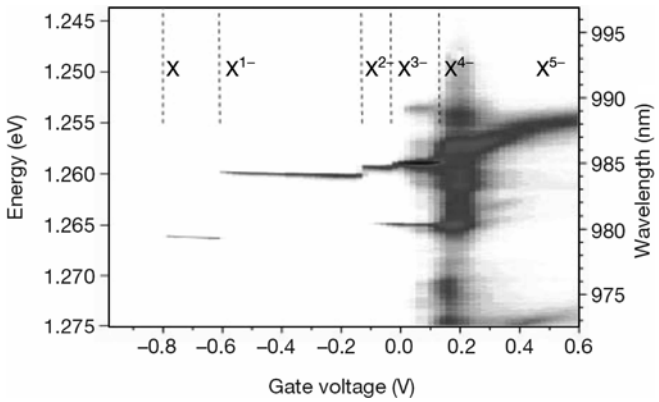

Fig. 13.34. Luminescence of charged excitons from a single quantum ring at $T = 4.2\,\mathrm{K}$ vs. the bias voltage with which the number of electrons in the quantum dot N is tuned from zero to $N>3$. Adapted from [910], reprinted with permission from Nature, ©2000 Macmillan Magazines Limited

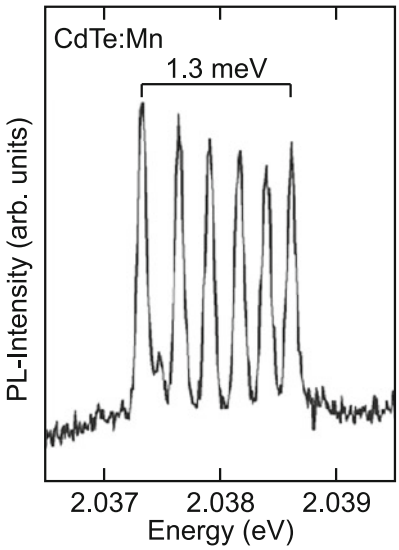

Fig. 13.35. Photoluminescence spectrum of a single CdTe/ZnSe quantum dot containing a single Mn atom ($T = 5\,\mathrm{K}$).

with the Mn $S = 5/2$ spin leads to a six-fold splitting of the exciton line (Fig. 13.35. In an external magnetic field a splitting into a total of twelve lines due to Zeeman effect at the Mn spin is observed.

In a QD ensemble, optical transitions are inhomogeneously broadened due to fluctuations in the QD size and the size dependence of the confinement

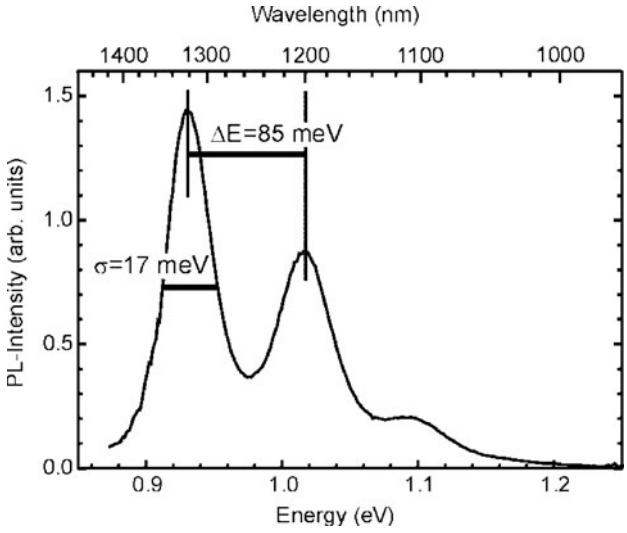

Fig. 13.36. Ensemble photoluminescence spectrum ($T = 293\,\mathrm{K}$, excitation density $500\,\mathrm{W/cm^2}$) of InAs/GaAs QDs

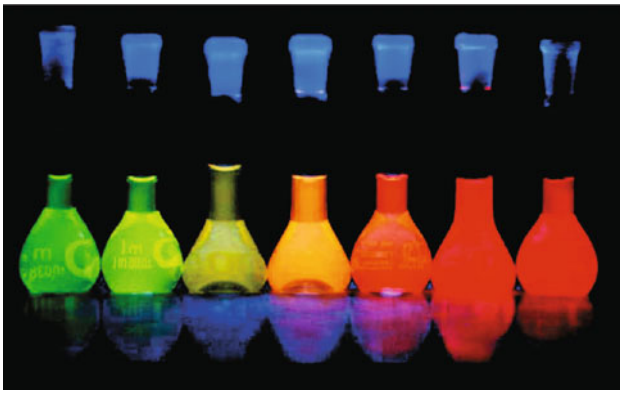

Fig. 13.37. Luminescence (under UV excitation) from flasks of colloidal CdTe quantum dots with increasing size (from left to right). From [892]

energies (Fig. 13.36). Interband transitions involving electrons and holes suffer from the variation of the electron and hole energies:

$$\sigma_E \propto \left(\left| \frac{\partial E_\mathrm{e}}{\partial L} \right| + \left| \frac{\partial E_\mathrm{h}}{\partial L} \right| \right) \delta L \; . \tag{13.17}$$

A typical relative size inhomogeneity of σ_L/L of 7% leads to several tens of meV broadening. Additional to broadening due to different sizes fluctuations of the quantum dot shape can also play a role. The confinement effect leads to an increase of the recombination energy with decreasing quantum-dot size. This effect is nicely demonstrated with colloidal quantum dots of different size as shown in Fig. 13.37.